

Structural evolution in LaCoO₃ by polyol treatment: Highly active and resistant Co₃O₄/La₂O₂CO₃/LaCoO₃ heterostructure catalysts for CH₄ oxidation

Yahan Wang^a, Saifei Wang^{a,*}, Jingyu Bai^a, Long Zhang^b, Shiguang Zhao^a, Jiguang Deng^b, Xiaolong Tang^c, Erhong Duan^{a,*}

^a School of Environmental Science and Engineering, Hebei University of Science and Technology, 26th Yuxiang Street, Shijiazhuang, Hebei 050018, China

^b School of Environmental and Chemical Engineering, Faculty of Environment and Life, Beijing University of Technology, Beijing 100124, China

^c School of Energy and Environmental Engineering, University of Science and Technology Beijing, Beijing 100083, China



ARTICLE INFO

Keywords:

Methane oxidation
Heterostructure catalysts
Highly resistant
Reactive oxygen species
Interfacial effects

ABSTRACT

The development of high-performance nonprecious metal catalysts that are resistant to water and poisoning is of great importance for industrial methane treatment and is challenging. Herein, we prepared a Co₃O₄/La₂O₂CO₃/LaCoO₃ heterostructure catalyst with excellent catalytic performance ($T_{90} = 476$ °C), resistance to water and resistance to poisoning using a simple solvent-thermal method. DFT calculations combined with experimental characterization demonstrated that La₂O₂CO₃ provides more reactive oxygen species (O[·] and O²⁻) to Co₃O₄ via charge transfer at the interface to enhance the oxidation of methane. Moreover, water and SO₂ could be preferentially adsorbed on La₂O₂CO₃ to protect the active site of Co₃O₄, which improved its poisoning tolerance. Correspondingly, the structure had more density states near the Fermi level and accelerated the electron transfer on the structural surface, which enhanced the adsorption and dissociation of oxygen and methane. This research provides a comprehensive understanding of the structure-performance relationship of heterogeneous structured catalysts in catalytic combustion.

1. Introduction

Different from coal and oil, natural gas produces less carbon dioxide during combustion and contains almost no harmful substances such as sulfur and dust, making it a clean alternative to other fossil fuels [1,2]. However, methane (CH₄), the main component of natural gas, is also the second most important greenhouse gas after carbon dioxide [3,4]. The greenhouse effect from CH₄ has contributed approximately 20% of global warming since the industrial revolution [5]. During the production, processing, storage and distribution of natural gas, small amounts of CH₄ are emitted into the atmosphere, which can cause a serious greenhouse effect [6,7]. Therefore, the removal of CH₄ emissions from these processes is extremely important to mitigate the greenhouse effect. Among the existing treatment technologies, catalytic combustion is considered to be the most promising CH₄ abatement technology because it can not only treat CH₄ at relatively low temperatures but also avoid secondary pollutants such as NO_x and CO [8,9]. However, water vapor and SO₂ are frequently present in exhaust gas fractions containing CH₄,

and these circumstances might lead to material deactivation. Catalytic materials with high performance, water and poisoning resistance are critical for achieving effective industrial CH₄ degradation [10].

In particular, Co³⁺/Co²⁺ ions in Co₃O₄-based catalysts in concert with surface oxygen vacancies efficiently activate molecular oxygen, resulting in the formation of electrophilic reactive oxygen species (O²⁻, O₂[·], and O[·], etc.) that enhance the chemisorption of alkane molecules and oxygen electron transfer processes to facilitate alkane catalytic reactions [11–13]. The CH₄ oxidation process inevitably involves water vapor, which can be readily adsorbed on the Co₃O₄ surface and rapidly dissociated, producing hydroxyl species that poison the catalyst active site, impeding the formation of carbonate species and deactivating Co₃O₄ [14,15]. Many studies have been conducted on how to improve the water resistance of Co₃O₄ while increasing its reactive oxygen content to further enhance its catalytic activity. For instance, Sun et al. [16] introduced Cu atoms into Co₃O₄-110 facets to induce the generation of defective structures, which accelerated the generation of reactive oxygen species and improved the catalytic activity of propane while

* Corresponding authors.

E-mail addresses: wang_saifei@163.com (S. Wang), duan_eh@163.com (E. Duan).

effectively enhancing the water resistance. Other scholars have also doped Mn atoms into Co_3O_4 -100 facets to improve the water resistance in the catalytic reaction of propane [17]. When the CH_4 emission gas is more complex, it is also accompanied by the emission of sulfur compounds. The emission of sulfur compounds can form sulfates and sulfites on the Co_3O_4 surface, poisoning the Co_3O_4 catalytic active site and preventing the production of reactive oxygen species, leading to catalyst deactivation [18,19]. Although the abovementioned atomic doping methods could improve the water resistance while effectively enhancing the catalytic activity, the improvement in the poisoning resistance remained very limited. However, combining with other oxides to form heterostructure catalysts can greatly improve this situation.

In heterogeneous catalysis, the heterogeneous interface formed by the metal/support is a key factor in improving the catalyst characteristics [20,21]. Therefore, it is essential to design catalysts with unique heterogeneous structures. As previously reported, oxide materials (e.g., CeO_2 [22], Al_2O_3 [23], CuO [24], etc.) have been widely used as matrices to support active metals to further enhance the catalytic performance of Co_3O_4 while providing water and poisoning resistance for demanding industrial systems. In particular, Al_2O_3 has been widely studied as a support that could trap sulfate species as sulfation carriers to protect the catalyst active site and slow the poisoning process [25]. Therefore, the selection of a carrier that can be sulfated is currently the most effective way to mitigate sulfur poisoning in Co_3O_4 -based catalysts. Yoon et al. [26] synthesized Co_3O_4 nanocubes (NCs) with controlled CeO_2 layers through a selective deposition protocol to investigate the role of heterogeneous interfaces in catalytic oxidation. The results showed that the addition of the CeO_2 layer provided sufficient oxygen to the Co_3O_4 surface so that the $\text{CeO}_2\text{-Co}_3\text{O}_4$ NCs heterostructure exhibited a higher CO oxidation rate and water resistance than that of the single-phase Co_3O_4 and demonstrated that the underlying cause for the enhanced characteristics of the structure was due to the charge transfer at the heterogeneous interface. In other studies, La-based oxides such as LaCO_3OH ($\text{Co}_3\text{O}_4/\text{LaCO}_3\text{OH}/\text{graphene oxide}$, sandwich-type composite oxide) and $\text{LaNi}_{0.5}\text{Co}_{0.5}\text{O}_{2.5}$ ($\text{Co}_3\text{O}_4/\text{LaNi}_{0.5}\text{Co}_{0.5}\text{O}_{2.5}$) were also used as Co_3O_4 oxygen supply catalyst additives [27,28]. In particular, the peroxide ($\text{O}_2^{\cdot-}$) in LaCO_3OH provided abundant active oxygen for Co_3O_4 to enhance the catalytic activity, while the structure also exhibited good thermal stability. These three papers show that the specific interactions of multiple metal oxides after forming heterostructures contribute to the improvement of Co_3O_4 catalytic performance and water resistance. However, its ability to tolerate poisoning still needs further investigation. The preparation of nanohybrid metal oxides has been widely reported, but the construction of heterogeneous structured metal oxide catalysts by efficient and simple methods is still very much needed [29]. Current research on Co_3O_4 -based catalysts is mostly focused on the oxide- Co_3O_4 heterogeneous interface. However, studies on the preparation, interfacial effects, and resistance of composites of carbonates (especially La-based carbonates) and Co_3O_4 are scarce. Meanwhile, the La-based carbonate- Co_3O_4 heterogeneous interface is also more complex than the oxide- Co_3O_4 interface, and the accurate characterization of this type of heterogeneous interface is also a challenging task. In our previous paper, we successfully prepared $\text{Co}_3\text{O}_4/\text{La}_2\text{O}_2\text{CO}_3/\text{LaCoO}_3$ heterostructure catalysts by using alkaline amino acid-based deep eutectic solvent (DES) for reaction with LaCoO_3 perovskite, which exhibited excellent methane catalytic activity [30]. However, in previous studies, we focused more on the catalytic performance of the catalyst, and the conformational relationship, oxidation mechanism and resistance to poisoning of the heterogeneous structure have not been explained and studied in detail.

In this work, we replaced the solvent with a simple and inexpensive alcohol solvent in the preparation of $\text{Co}_3\text{O}_4/\text{La}_2\text{O}_2\text{CO}_3/\text{LaCoO}_3$ heterostructure catalysts, which makes the preparation process more efficient and convenient. Furthermore, the excellent thermal stability, water resistance and resistance to poisoning exhibited by this heterostructure catalyst were systematically investigated, and their anti-poisoning

mechanism was explained. The catalyst was characterized in detail to gain insight into the growth process and physicochemical characteristics of the heterogeneous structure. In addition, the structure-function relationship between interfacial charge transfer and catalytic activity as well as the oxidation mechanism of CH_4 were revealed by combining $\text{Co}_3\text{O}_4/\text{La}_2\text{O}_2\text{CO}_3/\text{LaCoO}_3$ catalyst characteristics, *in situ* diffuse reflectance infrared Fourier transform spectroscopy (DRIFTS) data and density functional theory (DFT) simulations.

2. Materials and methods

2.1. Chemicals

All chemicals were analytical reagent (A.R.) grade and could be used as received. Cobalt nitrate ($\text{Co}(\text{NO}_3)_2\cdot 6 \text{H}_2\text{O}$, 99.0%), lanthanum nitrate ($\text{La}(\text{NO}_3)_3\cdot 6 \text{H}_2\text{O}$, 99.0%), citric acid (99.5%) and glycerol (99.0%) were purchased from Sinopharm Chemical Reagent Co. Ltd. (Shanghai, China).

2.2. Catalyst preparation

LaCoO_3 was prepared by the sol-gel method. The precursor solution was formed by dissolving $\text{La}(\text{NO}_3)_3\cdot 6 \text{H}_2\text{O}$ (0.04 mol), $\text{Co}(\text{NO}_3)_2\cdot 6 \text{H}_2\text{O}$ (0.04 mol) and citric acid (0.10 mol) in 40 mL of ultrapure water and stirring for 0.5 h at 40 °C to mix them completely. The temperature was increased to 80 °C and stirring was continued for 6 h to form the wet gel. Then the gel was dried at 90 °C for 8 h to form the dry gel. Finally, the obtained samples were ground and calcined at 800 °C (3 °C·min⁻¹) in an air atmosphere for 5 h. The final sample obtained was the LaCoO_3 sample, labeled as LC.

The prepared LaCoO_3 (0.01 mol), different amounts of glycerol (molar ratio between 0 and 1.1 for glycerol and Co) and 15 mL of ultrapure water were placed in a 50 mL Teflon-lined stainless-steel autoclave (HTG-200-SS1; Anhui Kemi Machinery Technology) and kept at 230 °C for 6 h. The products were collected by filtration and dried at 80 °C for 4 h. Finally, they were ground and calcined at 600 °C (3 °C·min⁻¹) in an air atmosphere for 1 h. The resulting catalysts were labeled LC-(x)C (x represents the molar ratio of Co to glycerol, x = 0.01, 0.05, 0.1, 0.3, 0.5, 0.7, 0.9, 1.1). To find the best modification solvent, solvothermal experiments with other alcohols (methanol, ethanol, ethylene glycol, isopropanol alcohol, propylene glycol, glycerol, 1-butanol, 1,4-butanediol and 1,2,4-butanetriol in a ratio of 0.9) were also performed and the resulting catalysts were labeled LC-y (y represents the name of the alcoholic solvent). The synthesis process of Co_3O_4 and $\text{La}_2\text{O}_2\text{CO}_3$ single-phase catalysts is shown in Appendix A Supplementary Data.

2.3. Catalyst characterization

Characterization methods include X-ray diffraction (XRD), Brunauer-Emmett-Teller (BET) analysis, scanning electron microscopy (SEM), transmission electron microscopy (TEM), X-ray spectroscopy unit (EDX), inductively coupled plasma optical emission spectrometry (ICP-OES), electron paramagnetic resonance (EPR) spectra, X-ray photoelectron spectroscopy (XPS), H_2 temperature-programmed reduction ($\text{H}_2\text{-TPR}$), O_2 temperature-programmed desorption ($\text{O}_2\text{-TPD}$), CO_2 temperature-programmed desorption ($\text{CO}_2\text{-TPD}$), thermogravimetric analysis (TGA), *in situ* diffuse reflectance infrared Fourier transform spectroscopy (DRIFTS) and density functional theory (DFT) calculations. The experimental parameters are detailed in Appendix A Supplementary Data.

2.4. Catalytic activity measurement

CH_4 catalytic activity evaluation experiments were tested at atmospheric pressure using a fixed-bed reactor (CPR-6060, Tianjin Xianquan

Industry & Trade Development Co. Ltd., Tianjin, China, size: length 50 cm × width 80 cm). For each test, 0.2 g of catalyst was mixed with quartz sand to 0.5 mL (both catalyst and quartz sand at 40–60 mesh) in a quartz tube reactor (i.d = 6 mm). The reaction gas was composed of 1.0 vol% CH₄, 5.0 vol% CO₂ (when used), 5 vol% H₂O (when used), 100 ppm SO₂ (when used) and 99.0 vol% Air. The water vapor was injected using a water bubbler. The flow rate of the reaction gas was controlled at 50 mL·min⁻¹ and the space velocity (SV) was 6000 h⁻¹. The inlet and outlet concentrations of CH₄ and CO₂ were analyzed by a gas chromatograph (GC7900, Tianmei (Holdings) Co. Ltd., Shanghai, China) equipped with a hydrogen flame ionization detector (FID). In addition, catalyst performance was tested at flow rates of 100, 150 and 200 mL·min⁻¹, which correspond to volume space velocities (GHSV) of 12,000, 18,000 and 24,000 h⁻¹. Data on the reaction kinetics are shown in Appendix A Supplementary Data.

3. Results and discussion

3.1. Material crystal structure and growth process

XRD was used to analyze the changes in the composition and crystal structure of the LaCoO₃ catalyst brought by the addition of different ratios of glycerol and different alcoholic solvents. Fig. 1a-b showed that small peaks with hexagonal La₂O₂CO₃ (PDF#37-0804) at 2θ = 25.8, 27.6 and 30.3° and small peaks with cubic Co₃O₄ (PDF#43-1003) at 2θ = 36.8° when hydrothermal reactions were conducted without the addition of glycerol. The generation of new phases indicates that a trace decomposition for LaCoO₃ also occurs by pure hydrothermal treatment. The intensity of the La₂O₂CO₃ and Co₃O₄ peaks gradually strengthened with increased glycerol ratios. Moreover, the intensity of the peaks at 2θ = 23.2, 32.9, 33.3, 40.7 and 47.5° hexagonal LaCoO₃ (PDF#48-0123) gradually weakened and disappeared completely when the ratio reached 0.1, and only the peak at 2θ = 59.7° was faintly retained. These results indicated that most of the perovskite precursors were dissolved and

chemically reacted to form new phases during the solvent-thermal process, and only trace amounts were retained. The specific content of each phase in LC-(x)C could be quantified by Rietveld refinement [31, 32], and it was found that after a ratio of 0.3, the sample contains only approximately 3.0 wt% of the LaCoO₃ species content (Table S1). The increase in the ratio of glycerol caused a gradual increase in the content of La₂O₂CO₃ and Co₃O₄ in the catalyst, while the content of LaCoO₃ decreased rapidly. After the ratio reaches 0.3, the physical phase no longer changes significantly and the peak corresponding to La₂O₂CO₃ becomes sharper with increasing glycerol ratio, indicating that La₂O₂CO₃ becomes more crystalline. This can be verified by calculating the grain size of La₂O₂CO₃ (Table S2). The XRD results of the prepared LC-y catalysts (Fig. S1) showed that solvent addition, except glycerol and 1,2,4-butanediol solvents, did not result in significant dissolution of LaCoO₃ perovskite, which may be related to the physicochemical properties of the solvents. Meanwhile, monomeric La₂O₂CO₃ and Co₃O₄ were also prepared hydrothermally using glycerol, and the XRD patterns are shown in Fig. S3.Scheme 1.

To further explain the growth process of the material, XRD tests were performed on the pre-calcined products (LC-(x)C-M) (Fig. S2 a-b). La(OH)₃, Co(OH)₂ and trace amounts of LaCO₃OH phases were all present in LC-(x)C-M. This indicated that glycerol could provide OH⁻ to dissolve more LaCoO₃ structures during the solvent-thermal process, and the dissolved La³⁺ and Co²⁺ combined with OH⁻ in water and glycerol to form La(OH)₃ and Co(OH)₂. The LaCO₃OH phase was generated due to the high sensitivity of La(OH)₃ to CO₂, which reacts with trace amounts of CO₂ in the reactor at lower temperatures [33]. Therefore, the main reaction equation occurring during the solvent-thermal process was:

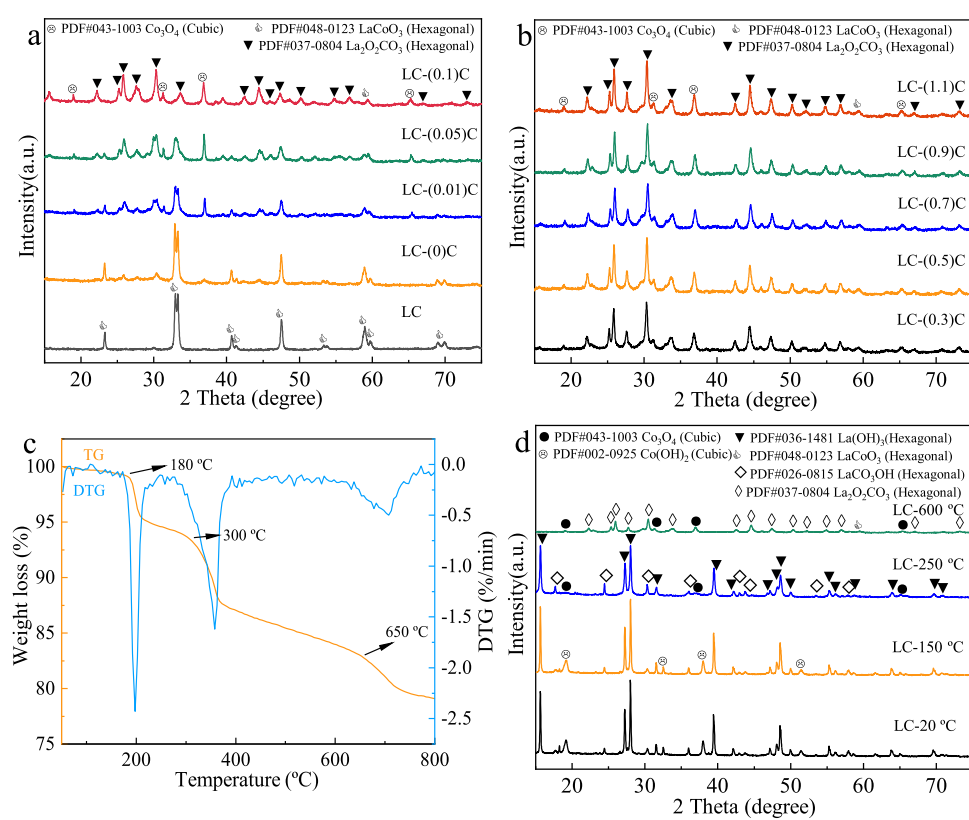
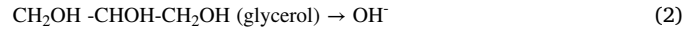
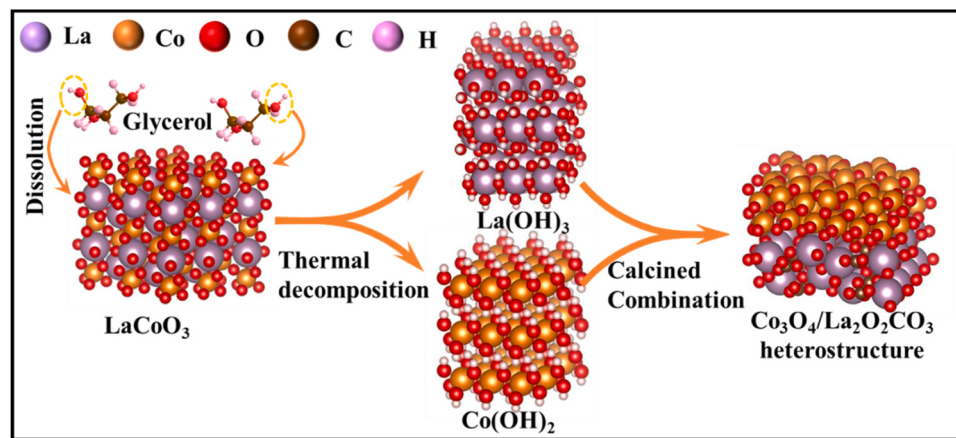
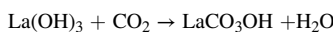
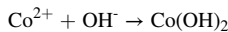


Fig. 1. (a, b) XRD patterns of LC-(x)C (x = 0–1.1), (c) TG and DTG curves profiles of LC-(0.9)C-M, (d) XRD patterns of LC-T (T = 150, 250 and 600 °C).



Scheme 1. Fabrication route for Co₃O₄/La₂O₂CO₃ heterostructure catalysts.



Glycerol was a solvent with strong reducing properties, which could reduce the dissolved Co³⁺ in LaCoO₃ perovskite to Co²⁺ at high temperature, and then further react with OH⁻ to form Co(OH)₂. However, there is inevitably a partial loss of Co³⁺ in the process. The ICP results demonstrated that the content of Co ions in LC-(0)C and LC-(0.9)C was significantly decreased. According to investigations, the existence of OHCO₃²⁻ and CO₃²⁻ could be detected when La(OH)₃ was heated in air [34, 35]. TG-DTG tests were performed on LC-(0.9)C-M under an air atmosphere to further explain the La(OH)₃ and Co(OH)₂ transformation process to La₂O₂CO₃ and Co₃O₄ during calcination. The calcination could be divided into three stages before 600 °C, with a temperature point determined at each stage for post-calcination XRD testing to observe the phase changes (Fig. 1 c-d). H₂O was the only product observed before 600 °C. There was no change in the physical phase in the XRD pattern corresponding to the first stage, so this stage was mainly the removal of surface water from the material. The Co(OH)₂ phase was no longer observed in the second stage, and the intensity of the LaCO₃OH phase peak increased and La(OH)₃ weakened. This result indicated that Co(OH)₂ reacted to generate Co₃O₄ and part of La(OH)₃ formed LaCO₃OH in this phase, and no bulk carbonation occurred. In the third stage, all La(OH)₃ and LaCO₃OH have been reacted to La₂O₂CO₃. These results indicated that La(OH)₃ would fully absorb CO₂ from the air when drying, and then convert to LaCO₃OH with increasing temperature, which was relatively slow at the lower temperatures. As the temperature increases LaCO₃OH further reacts to form La₂O₂CO₃. Therefore, the main reaction equation that occurs during the calcination was:



3.2. Material texture characteristics

All LC-(x)C catalysts showed typical type IV isotherms with hysteresis loops belonging to type H3 (Fig. S4), implying the existence of different mesoporous structures with lamellar particle accumulation for all catalysts [36–38]. Notably, LC-(0)C had the largest specific surface area (S_{BET}, 31.6 m²·g⁻¹) and pore volume (V_P, 0.37 cm³·g⁻¹), demonstrating that hydrothermal treatment could greatly enhance the S_{BET} (9.7 m²·g⁻¹) of LaCoO₃ (Table S2). With the addition of glycerol, the S_{BET} for LC-(x)C catalysts exhibited a trend of decrease followed by a

slight increase. This phenomenon may be attributed to the massive dissolution of the LaCoO₃ precursor, and the pore structure formed during the solvent-thermal process was gradually blocked by the generated La₂O₂CO₃ and Co₃O₄, leading to the formation of larger flakes or particles. The slight increase in subsequent S_{BET} may be due to the increase in the glycerol ratio, the better crystalline shape of the generated La₂O₂CO₃ and the generation of a new pore structure [39].

The morphological and structural characteristics of LC-(x)C catalysts were studied by SEM and TEM techniques. The SEM images of the prepared material, as shown in Fig. S5, showed that LaCoO₃ was composed of a large number of elliptical particles stacked in the size range of 50–150 nm. After hydrothermal treatment LC-(0)C turned into a stack of smooth flakes with sizes between 100 and 200 nm. The lamellar structure of LC-(0.05)C became thick and rough after the addition of trace amounts of glycerol, while multiple morphological random compositions (elliptical particles and lamellar) could be observed for LC-(0.9)C due to the multiphase intergrowth. The changed morphological structure for the catalysts was consistent with the results of the BET analysis described above. The lattice sizes in the HRTEM images (Fig. 2 a-c) match well with LaCoO₃, Co₃O₄ and La₂O₂CO₃ species. Among them, LC-(0)C and LC-(0.05)C had major exposure plane spacings of 0.223 nm, 0.279 nm and 0.265 nm corresponding to LaCoO₃ crystalline phases (202), (110) and (104) facets; 0.394 nm, 0.312 nm and 0.297 nm belonged to La₂O₂CO₃ crystalline phases (004) and (103) facets, respectively. The La₂O₂CO₃ ($d_{(101)} = 0.347$ nm) and Co₃O₄ ($d_{(220)} = 0.286$ nm) phases in LC-(0.9)C were the main crystalline phases of this catalyst. Additionally, the Fast Fourier Transform (FFT inset) showed a polycrystalline diffraction ring pattern. According to the elemental mapping scan (Fig. 2 d-m), the detailed distribution states of La, Co, O and C elements could be clearly observed. Each element was uniformly distributed on the material surface, except for the partial aggregation of Co. The above results imply that the nanocrystal structures of the phases were well combined.

3.3. Material surface chemical properties

The surface elemental composition and chemical state of the LC-(x)C catalysts were characterized by XPS. As shown in Table S3, the LC-(0.9)C surface Co/La atomic ratio (A_{XPS}) (0.73) was significantly higher than that of the other catalysts, which indicated that more Co species covered the catalyst surface. The Co 2p spectra showed two main peaks, Co 2p_{3/2} and Co 2p_{1/2} and could be decomposed into Co³⁺ and Co²⁺ spin doublets at binding energies (BEs) [40,41]. LC-(0.9)C had the highest Co³⁺/Co²⁺ (1.42). Co³⁺ species have been reported to act as active sites in catalytic reactions and to improve oxygen activation and migration, thus enhancing the adsorption and dissociation of C-H bonds [42,43]. The Co 2p orbital binding energy was transferred to a lower energy, which

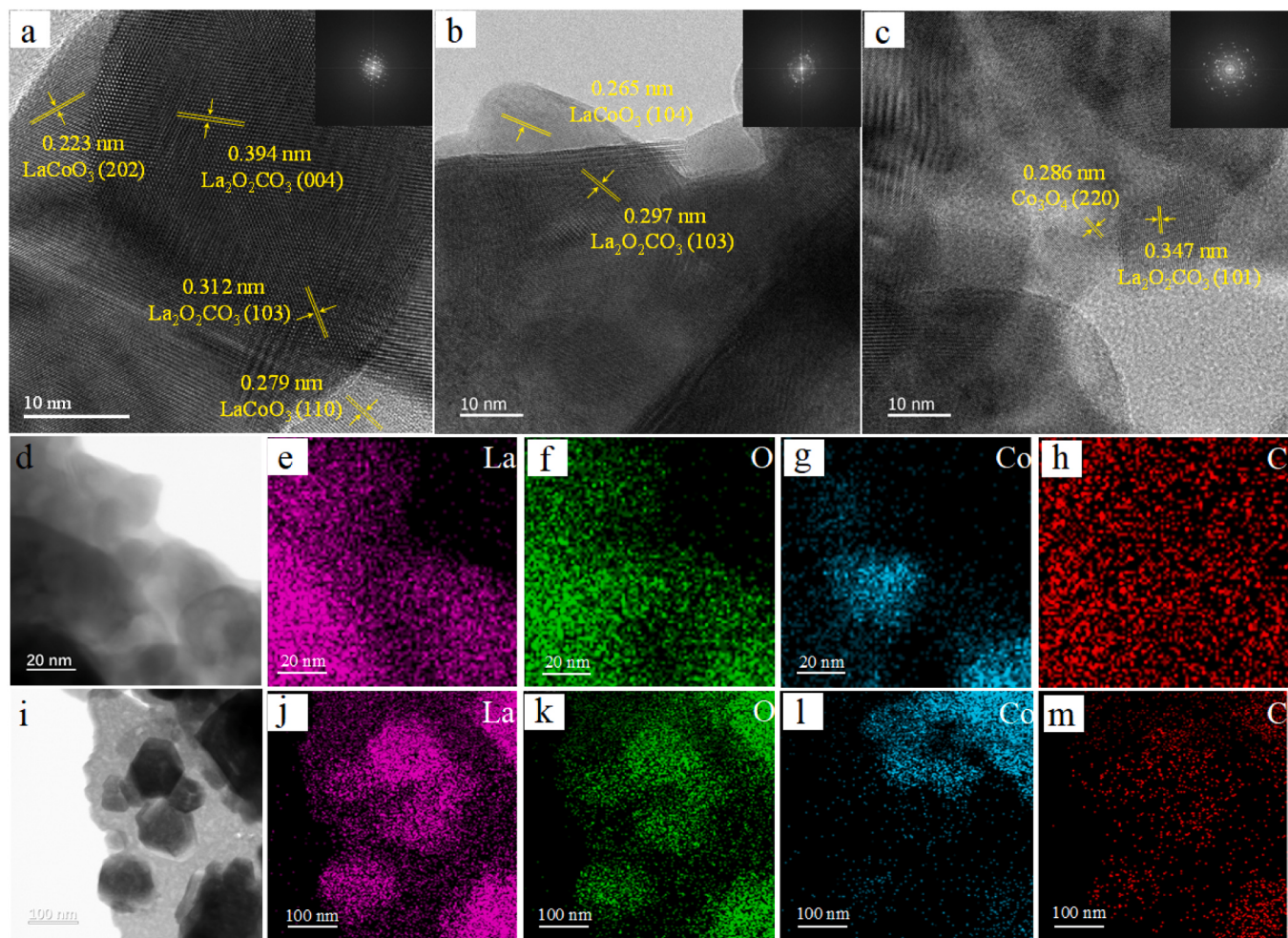


Fig. 2. HRTEM images of (a) LC-(0)C, (b) LC-(0.05)C and (c) LC-(0.9)C. Element mapping of (d-h) LC-(0.05)C and (i-m) LC-(0.9)C.

indicated that there would be an electron transfer to Co₃O₄ in this heterogeneous structure. It also demonstrated the reduction of the Co-O bonding energy. O 1 s spectra showed that the peaks at binding energies (BEs) of 528.5–529.2 eV were attributed to lattice oxygen species (O²⁻), 529.5–531.0 eV to peroxides (O⁻), 531.1–531.9 eV to CO₂²⁻ and 531.8–532.9 eV to superoxide (O₂) [44,45]. The O 1 s orbital binding energy of LC-(0.9)C showed a large change compared to that of monomeric LaCoO₃, Co₃O₄ and La₂O₂CO₃, with all oxygen species binding energies shifting to lower energies. This was caused by strong interfacial interactions, demonstrating that the formation of Co₃O₄ and La₂O₂CO₃ led to a change in the electronic structure of the catalyst surface. LC-(0.9)C had the largest (O⁻+O₂)/O²⁻ ratio (Table 1), indicating that LC-(0.9)C had the most active adsorbed oxygen. Combined with the XRD results, it was demonstrated that the presence of La₂O₂CO₃ facilitated

the generation of active adsorbed oxygen on the catalyst surface. The catalyst surface adsorbed oxygen was related to the capture of CH₄ and activation of gaseous oxygen, which was necessary for catalyst oxidation, so the high adsorbed oxygen content was beneficial for CH₄ adsorption and conversion [46].

The adsorbed oxygen was closely related to the formation of oxygen vacancies, so the adsorbed oxygen content was often used to evaluate the content of oxygen vacancies on the catalyst surface [47]. Low-temperature electron paramagnetic resonance spectroscopy (EPR) was directly demonstrated and measured for the characterization of oxygen vacancies (V_O) in the catalyst (Fig. 3c). Therefore, the oxygen vacancies in LC, LC-(0)C and LC-(0.9)C were investigated in depth. At approximately $g = 2.003$, significant EPR signals can be observed for LC-(0)C and LC-(0.9)C, which could correspond to defective oxygen species in the catalyst (i.e., O⁻ and O₂), demonstrating the presence of oxygen vacancies [48]. Meanwhile, LC did not exhibit any significant peak signal in the EPR pattern, indicating that no oxygen vacancies existed in LC or that the oxygen vacancy content was too low to be effectively monitored. In addition, the quantitative results showed that the oxygen vacancy concentration in LC-(0.9)C ($\sim 1.5 \times 10^{14}$ spins·g⁻¹) was significantly higher than that in LC-(0)C ($\sim 1.0 \times 10^{14}$ spins·g⁻¹). The above results indicated that the large production of La₂O₂CO₃ and Co₃O₄ facilitated the formation of surface oxygen defects and thus the CH₄ oxidation reaction. Meanwhile, the LC-(x)C catalyst was tested for CO₂-TPD. Considering that the La₂O₂CO₃ pyrolysis present in the LC-(0.9)C catalyst also produces CO₂, thermogravimetric analysis (TGA) tests were performed to probe the pyrolysis temperature of the LC-(0.9)C

Table 1
XPS results of LC-(x)C catalysts.

Sample	Co ³⁺ / Co ²⁺	(O ⁻ +O ₂ ⁻)/O ²⁻	Binding energy (eV)			
			Co ³⁺	Co ²⁺	Co ³⁺	Co ²⁺
			(2p _{3/2})	(2p _{3/2})	(2p _{1/2})	(2p _{1/2})
LC	1.06	1.11	780.3	781.4	795.5	796.6
Co ₃ O ₄	1.37	0.62	780.3	781.4	794.4	796.6
La ₂ O ₂ CO ₃	-	2.00	-	-	-	-
LC-(0)C	1.38	1.67	779.5	780.8	794.6	796.1
LC-(0.05)C	1.40	3.04	779.7	781.3	794.7	796.1
LC-(0.9)C	1.42	6.10	779.3	780.6	794.5	796.0

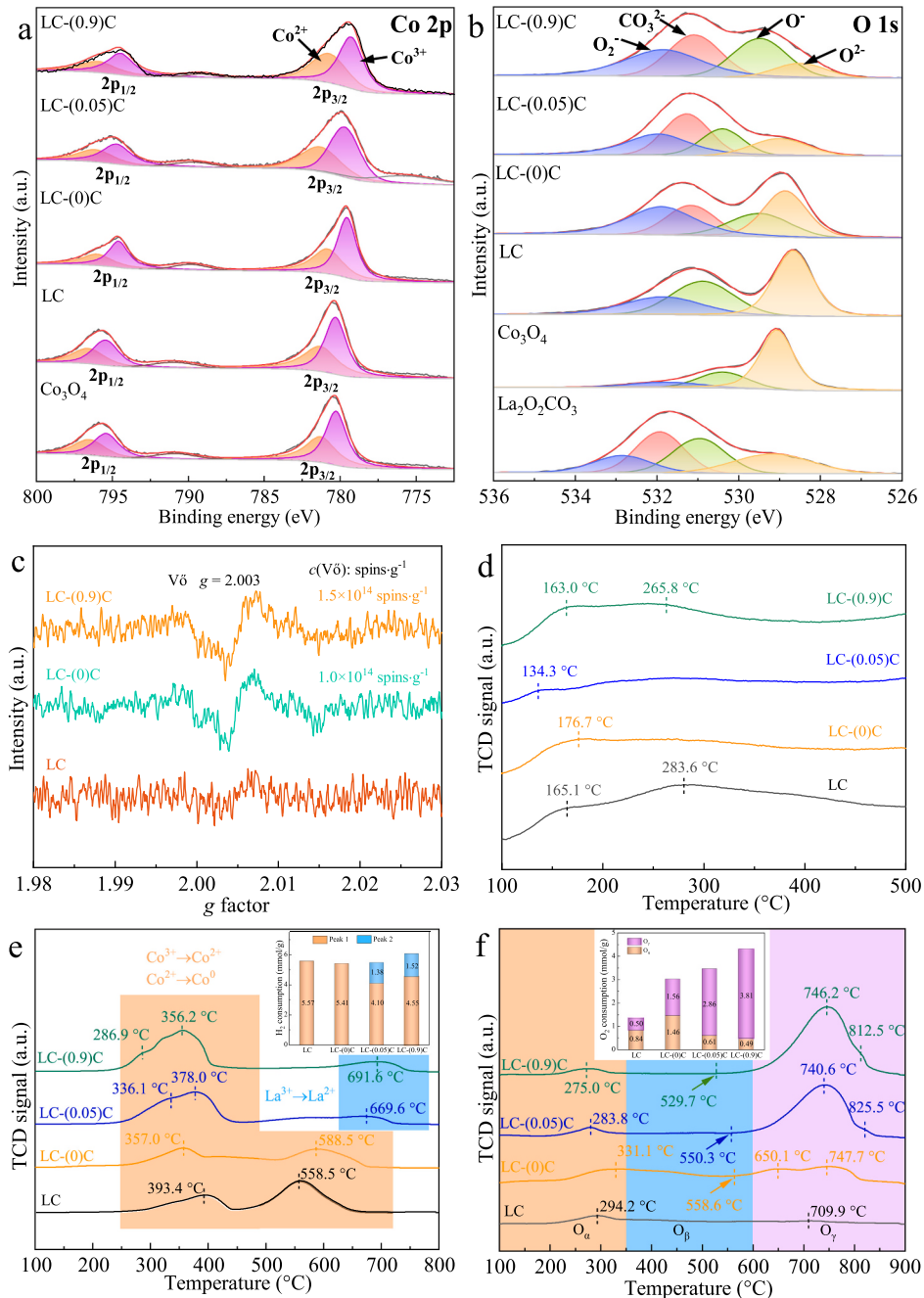


Fig. 3. (a) Co 2p, (b) O 1s spectra, (c) EPR spectra profiles, (d) CO₂-TPD spectra, (e) H₂-TPR spectra and (f) O₂-TPD spectra for LC-(x)C catalysts.

catalyst. As shown in Fig. S6, the LC-(0.9)C catalyst could be stable until 642 °C. This result demonstrated that LC-(0.9)C exhibited the best CO₂ adsorption capacity at low temperatures (Fig. 3d), and the alkalinity of the material was enhanced by the glycerol treatment. The alkaline site had strong electrophilicity, which would increase the alkaline oxygen ions (O₂⁻, O²⁻ and O⁻, etc.) on the catalyst surface to a certain extent, which might be related to the formation of La₂O₂CO₃ [49,50]. According to a previous study, the unique La³⁺-O²⁻ pair sites of La₂O₂CO₃ contributed to basic adsorption site formation on the catalyst [51]. Moreover, CO₂ was found to have a thermodynamically and kinetically higher affinity for lanthanide oxides, which facilitates chemisorption on their surface to form carbonate species [52,53]. Gaseous oxygen could react with carbonate species to form reactive oxygen species (O₂, O²⁻ and O⁻, etc.). Therefore, we designed to pretreat the LC-(0.9)C catalyst with a 5 vol% CO₂-95 vol% He atmosphere at 300 °C before performing the

O₂-TPD test. The test results are shown in Fig. S7, where the content of reactive oxygen species was increased in the sample after CO₂ pretreatment. This result confirmed that the interaction of adsorbed CO₂ with gaseous oxygen in the presence of La₂O₂CO₃ could promote the generation of reactive oxygen species. In general, the active oxygen source of this catalyst was generated by oxygen vacancies and CO₂ adsorption by La₂O₂CO₃.

The reduction of LC-(x)C catalysts was investigated by H₂-TPR. As shown in Fig. 3e, the reduction peaks of all samples could be assigned to three reduction reactions: Co³⁺ → Co²⁺ → Co⁰, and La³⁺ → La²⁺ [54, 55]. These three reduction reaction processes were compared with the H₂-TPR results for monomeric La₂O₂CO₃ and Co₃O₄ (Fig. S8a), thus further de-identifying the reaction processes. After the solvent-thermal treatment, all Co₃O₄ reduction peaks were shifted to low temperatures except for the Co²⁺ reduction peak of LC-(0)C. Specifically, after the

addition of glycerol, the Co^{2+} reduction peaks shifted significantly to low temperatures due to the large production of Co_3O_4 and $\text{La}_2\text{O}_2\text{CO}_3$, and the La^{3+} reduction peaks appeared. The La^{3+} reduction peak shifted toward high temperature after the increase in glycerol ratio, revealing a strong interaction between Co_3O_4 and $\text{La}_2\text{O}_2\text{CO}_3$, which made $\text{La}_2\text{O}_2\text{CO}_3$ become less reducible. Meanwhile, the lower reduction peak of LC-(0.9)C means a higher reactivity of oxygen and excellent oxidation performance [56,57]. O₂-TPD was used to characterize the oxygen species in the catalyst (Fig. 3f). Three oxygen desorption regions could be classified based on temperature: RT–350 °C (O_{α} , surface physical/chemical adsorbed oxygen), 350–600 °C (O_{β} , surface lattice oxygen) and > 600 °C (O_{γ} , bulk lattice oxygen) [58,59]. The presence of O_{β} peaks was not observed in these samples. The desorption temperature for the O_{α} peak decreased after the addition of glycerol, indicating that the interaction between $\text{La}_2\text{O}_2\text{CO}_3$ and Co_3O_4 could enhance the mobility of O_{α} . The O_{γ} peak of LC-(0.9)C was significantly enhanced. The O₂-TPD results for monomeric $\text{La}_2\text{O}_2\text{CO}_3$ and Co_3O_4 (Fig. S8b) revealed that the lower temperature peaks in the O_{γ} peak region were brought about by the $\text{La}_2\text{O}_2\text{CO}_3$ generation and the higher temperature peaks were brought about by the Co_3O_4 generation. Moreover, the initial oxygen release temperature of the O_{γ} peak shifted from 559 °C to 530 °C under

the two-phase interaction. This means that the interaction between $\text{La}_2\text{O}_2\text{CO}_3$ and Co_3O_4 after generation could also reduce the lattice oxygen bonding strength, enhance the diffusion of oxygen ions, and promote the movement and desorption of lattice oxygen [60].

The decreased lattice oxygen bonding energy may weaken the Co-O bonding energy. Therefore, the bonding properties of the samples were further discussed through Raman spectroscopy (Fig. S9a). One could observe that all bands of LC-(0.9)C became wider and significantly weaker in intensity compared to the Raman bands of monomeric LaCoO_3 , Co_3O_4 and $\text{La}_2\text{O}_2\text{CO}_3$, which may be related to the weakening of the bond energy of Co and La. The Raman band near 681 cm⁻¹ corresponds to the stretching vibration (V_s) of the six-coordinated Co-O bond in the octahedral gap, and the peak position shows a significant blue shift. To evaluate the Co-O bond strength, the bond force constant (k) was calculated from Hooke's law [56,61]. The calculated results are shown in Fig. S9b. LC-(0.9)C has the smallest Co-O bond force constant (321.9 N·m⁻¹), implying a weak Co-O bond. According to previous studies, the weakening of the Co-O bond could cause a decrease in oxygen desorption temperature and an increase in redox properties, which could correspond well with the above characterization [59].

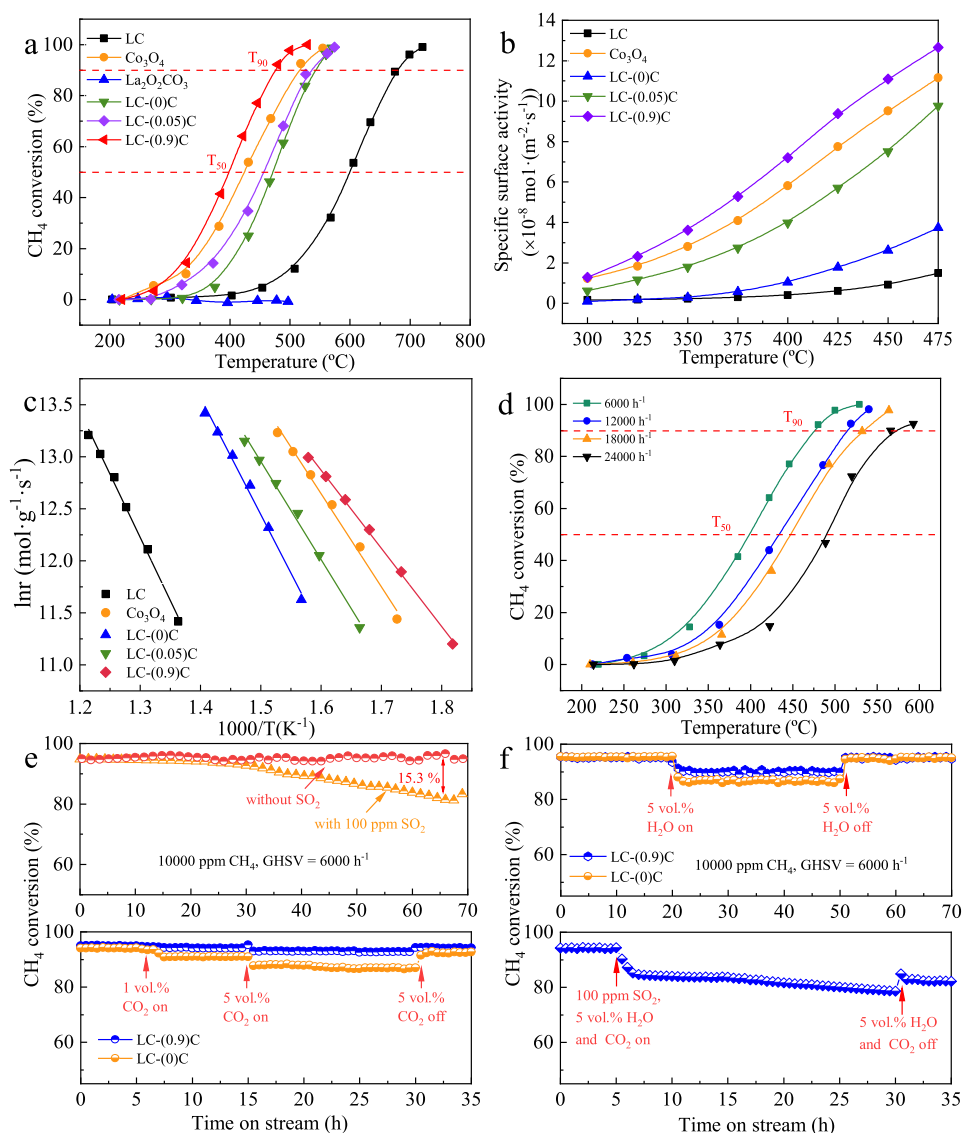


Fig. 4. (a) Methane conversion, (b) specific surface activity, (c) Arrhenius plots for different catalysts, and (d) conversion of LC-(0.9)C at different WHSV, (e) long-term stability, resistance to poisoning and CO_2 of LC-(0.9)C, (f) water vapor resistance test.

3.4. Catalytic performance and kinetic parameters

To explore the effect of alcoholic solvents and ratios on catalytic activity, the performance of the catalysts was evaluated at T_{50} and T_{90} , which are the temperatures of conversion of CH_4 at 50% and 90%, respectively (Fig. S10 and S11). It was found that compared to other solvents, the catalyst exhibited the best activity with glycerol as the solvent and at an addition ratio of 0.9 (LC-(0.9)C). As shown in Fig. 4a, the temperature at which LC-(0.9)C achieved 90% CH_4 conversion was only 476 °C, the temperature being 203 °C lower than the T_{90} of LaCoO_3 (679 °C), 66 °C lower than the T_{90} of LC-(0)C (542 °C), and 59 °C lower than that of LC-(0.05)C (535 °C). In addition, to evaluate the catalytic activity even further, the specific surface activity of each catalyst was calculated by a standardized comparison of surface areas. The CH_4 consumption rate of LC-(0.9)C ($3.61 \times 10^{-8} \text{ mol} \cdot \text{m}^{-2} \cdot \text{s}^{-1}$) at 350 °C was 13 times higher than that of LC-(0)C and LaCoO_3 , and twice as high as that of LC-(0.05)C (Table 2). The specific surface activity of LC-(0.9)C was much higher than that of the other catalysts (Fig. 4b). Furthermore, the apparent activation energy of the catalyst was calculated at low CH_4 conversions (0–20%) by using the values of the Arrhenius plot (Fig. 4c). LC-(0.9)C also showed the lowest activation energy ($E_a = 62.45 \text{ kJ} \cdot \text{mol}^{-1}$) with the strongest CH_4 activation, which was in good agreement with the order of catalytic activity. The order of activation energy from low to high was: LC-(0.9)C ($62.45 \text{ kJ} \cdot \text{mol}^{-1}$) < Co_3O_4 ($74.41 \text{ kJ} \cdot \text{mol}^{-1}$) < LC-(0.05)C ($78.38 \text{ kJ} \cdot \text{mol}^{-1}$) < LC-(0)C ($92.33 \text{ kJ} \cdot \text{mol}^{-1}$) < LC ($100.91 \text{ kJ} \cdot \text{mol}^{-1}$). The catalytic activity of monomeric Co_3O_4 and $\text{La}_2\text{O}_2\text{CO}_3$ was tested, and found that $\text{La}_2\text{O}_2\text{CO}_3$ did not exhibit catalytic activity up to 500 °C. Although Co_3O_4 showed better catalytic activity, it was not as good as LC-(0.9)C.

The effect of the CH_4 flow rate change on the catalytic performance was highly significant, and when the flow rate was increased, the residence time of CH_4 in the catalyst bed was shortened, resulting in a lower conversion rate. Therefore, the effect on the catalytic activity for LC-(0.9)C under different GHSV conditions was investigated. As expected, the CH_4 catalytic activity decreased to some extent when the GHSV was increased but still had excellent catalytic activity. Similarly, LC-(0.9)C could still exhibit excellent catalytic performance when compared with the catalyst performance in other studies (Table S9). This indicated that LC-(0.9)C was a promising catalyst, which was significant for industrial applications.

The stability of LC-(0.9)C was a concern due to the large amount of $\text{La}_2\text{O}_2\text{CO}_3$ contained in the LC-(0.9)C catalyst structure. In Fig. S6, the pyrolysis temperature of the LC-(0.9)C catalyst was 642 °C, which was much higher than the reaction temperature of the catalyst. Meanwhile, as shown in Fig. 4e, the catalyst exhibited excellent long-term stability, and the CH_4 conversion was still stable at 95% in the presence of 480 °C for 70 h. The XRD pattern of LC-(0.9)C after 70 h of testing showed a significant decrease in all diffraction peaks compared to the fresh catalyst (Fig. S13). The catalyst was exposed to high temperatures for a long time, which caused the catalyst grain size to decrease, the grains to become more disordered and the grain boundaries to increase. However, the composition of the physical phase of the catalyst did not change before and after the reaction, demonstrating that LC-(0.9)C had a highly stable structure. It was known that the CH_4 treatment process may be

accompanied by the presence of trace amounts of SO_2 , which might compete with the reactants for the adsorption active sites, causing a rapid decrease in activity and triggering sulfur poisoning. Therefore, the LC-(0.9)C catalyst was exposed to 100 ppm SO_2 to evaluate the catalyst's tolerance to sulfur poisoning. The CH_4 conversion was found to decrease only from 95% to 81% after 70 h of reaction at 485 °C, which indicated that the catalyst had excellent SO_2 tolerance. A large amount of $\text{La}_2(\text{SO}_4)_3$ appeared in the XRD pattern after the sulfur poisoning test (Fig. S14), which was generated by SO_2 adsorption on the surface of $\text{La}_2\text{O}_2\text{CO}_3$ in the reaction. This demonstrated that SO_2 would preferentially adsorb on $\text{La}_2\text{O}_2\text{CO}_3$, reducing the competitive adsorption with the reactants at the active site and making the catalyst more resistant to poisoning. $\text{La}_2\text{O}_2\text{CO}_3$ exhibited a protective effect while providing active oxygen to Co_3O_4 . Additionally, the conversion of $\text{La}_2\text{O}_2\text{CO}_3$ to $\text{La}_2(\text{SO}_4)_3$ reduces the adsorption of SO_2 and the formation of reactive oxygen species, which explains the decreased activity of this catalyst.

Water was always present in the CH_4 combustion exhaust gas. Therefore, water resistance testing of the catalyst was necessary. Water resistance tests were carried out in the presence of 5 vol% H_2O in the LC-(0.9)C catalyst (Fig. 4f). When 5 vol% H_2O was introduced, the CH_4 conversion dropped from 95% to 89% and remained at almost 89% for the next 30 h. The water resistance (8% decrease in CH_4 conversion) was significantly improved compared to the LC-(0)C catalyst. Subsequently, after stopping the introduction of H_2O , the CH_4 conversion could be recovered rapidly and still showed excellent stability. These results demonstrated that increasing the $\text{La}_2\text{O}_2\text{CO}_3$ content of this structured catalyst improved its water resistance. Furthermore, it indicated that the effect of water on the catalytic performance of LC-(0.9)C was minor and reversible. The slight decrease in activity was probably attributed to the competitive adsorption of CH_4 and water molecules at the active site from the catalyst, which disappeared after water was not introduced [62]. In addition to the resistance to water vapor and SO_2 , the effect of CO_2 on the catalyst needs to be considered. Prolonged exposure of catalysts to CO_2 could lead to the accumulation of carbonate species on the surface blocking the active site, which has been a problem that cannot be ignored. However, the LC-(0.9)C catalyst was stable after a slight decrease with the introduction of 1 vol% CO_2 and 5 vol% CO_2 . The activity could quickly return to normal after stopping the infusion. However, the LC-(0)C catalyst showed a more significant decrease. The excellent stability of the LC-(0.9)C catalyst under CO_2 was attributed to the unique $\text{La}^{3+}\text{-O}^{2-}$ alkaline adsorption site of $\text{La}_2\text{O}_2\text{CO}_3$, which could consume carbonate and form a dynamic equilibrium on the catalyst surface, avoiding the excessive accumulation of carbonate on the catalyst surface. The catalyst could react with oxygen to rapidly consume the surface carbonate to restore activity after stopping the inlet. To more completely evaluate the LC-(0.9)C catalyst under realistic conditions, simultaneous introduction of SO_2 , CO_2 and water vapor into the gas composition was performed in the CH_4 stability test. The catalytic activity showed a very significant decrease when the mixture was introduced. Moreover, the CH_4 conversion of LC-(0.9)C decreased from 95% to 78% after 25 h of gas mixture introduction. The catalytic activity was restored to 84% after stopping the passage of CO_2 and water vapor, and the decrease in catalytic activity was also slowed down. This means that although the catalyst deactivation was accelerated in the presence of SO_2 , CO_2 and water vapor, LC-(0.9)C still exhibited excellent resistance. The LC-(0.9)C catalyst not only possessed excellent catalytic performance, but also showed good stability under various conditions.

For heterostructure catalysts, the number of active sites, active oxygen content and redox ability are the main reasons for the catalytic performance [24,60,62]. A large amount of $\text{Co}(\text{OH})_2$ and $\text{La}(\text{OH})_3$ were generated by glycerol-induced LaCoO_3 pyrolysis, which formed a $\text{Co}_3\text{O}_4/\text{La}_2\text{O}_2\text{CO}_3/\text{LaCoO}_3$ heterostructure catalyst after calcination. This structure exposed more active Co species in higher valence states on the catalyst surface, which provided more active sites for the reactants. Meanwhile, the large number of surface oxygen vacancies generated during the growth and interaction between $\text{La}_2\text{O}_2\text{CO}_3$ and Co_3O_4

Table 2

Catalytic activity (T_{50} , T_{90}), reaction rate (r , at 350 °C), specific surface activity (SSA, at 350 °C) and activation energy (E_a) of LC-(x)C catalysts.

Sample	T_{50} (°C)	T_{90} (°C)	$r \times 10^{-7}$ ($\text{mol} \cdot \text{g}^{-1} \cdot \text{s}^{-1}$)	$\text{SSA} \times 10^{-8}$ ($\text{mol} \cdot \text{m}^{-2} \cdot \text{s}^{-1}$)	E_a ($\text{kJ} \cdot \text{mol}^{-1}$)
LC	599	679	0.22	0.26	100.91
Co_3O_4	423	516	2.69	2.80	74.41
LC-(0)C	471	542	0.88	0.28	92.33
LC-(0.05)C	456	535	0.33	1.80	78.38
LC-(0.9)C	398	476	3.75	3.61	61.45

enhanced the adsorption capacity of oxygen molecules, thus activating more gaseous oxygen to generate reactive oxygen and accelerating the catalytic reaction [37,43]. The unique $\text{La}^{3+}\text{-O}^2$ -alkaline adsorption site of $\text{La}_2\text{O}_2\text{CO}_3$ could provide a certain amount of reactive oxygen for the catalytic reaction, and the oxygen mobility was also improved by the multiphase interaction (demonstrated by O_2 -TPD). The redox ability of Co-based catalysts could be influenced by the redox cycle between Co^{3+} and Co^{2+} ions [44,63]. The high $\text{Co}^{3+}/\text{Co}^{2+}$ molar ratio and high active oxygen content of this catalyst could reduce the redox potential between ions, which accelerated the cyclic reaction and improved the redox ability of the catalyst. The trend of the LC-(x)C catalyst specific surface area did not correspond to the catalyst activity. However, the calculated specific surface activity by normalizing the specific surface area was consistent with the catalytic activity, indicating that the generation of $\text{La}_2\text{O}_2\text{CO}_3$ and Co_3O_4 could provide more catalytically active sites for the reaction with CH_4 compared to the increase in specific surface area. Furthermore, this result demonstrates that the specific surface area is not the main factor affecting the catalytic activity. The catalytic activity and above characterization confirmed that Co_3O_4 was the main active phase in the catalytic reaction, and $\text{La}_2\text{O}_2\text{CO}_3$ could act as both a donor to provide more reactive oxygen species for Co_3O_4 to promote the catalytic reaction and to protect Co_3O_4 in the presence of SO_2 . This also explained that LC-(0.9)C possessed more active sites and better CH_4 catalytic performance despite its lower specific surface area.

3.5. Density functional theory calculation

The above characterization clarified that this heterostructure catalyst had Co_3O_4 as the main active phase and $\text{La}_2\text{O}_2\text{CO}_3$ as the oxygen donor additive. However, the structure-function relationship for this heterogeneous structured catalyst and the intrinsic mechanism for the enhanced catalytic activity still need further explanation. Therefore, the

structure was investigated in depth by density functional theory (DFT) calculations. The DFT models for Co_3O_4 (110) and Co_3O_4 (110)/ $\text{La}_2\text{O}_2\text{CO}_3$ (101) are shown in Fig. 5a-b. The dissociative adsorption of CH_4 on the catalyst surface was considered to be the first and important step of the catalytic reaction. It was calculated that $\text{Co}_3\text{O}_4/\text{La}_2\text{O}_2\text{CO}_3$ exhibited lower CH_4 adsorption energy than Co_3O_4 (Fig. 5d). The adsorption energy for CH_4 on the Co_3O_4 surface was 0.94 eV, which decreased significantly to 0.77 eV after forming a heterogeneous structure with $\text{La}_2\text{O}_2\text{CO}_3$. Depending on the adsorption energy definition, although the adsorption state was still unstable, the results showed that heterogeneous structure formation enhanced the adsorption of CH_4 , which indicated that more electrons could be transferred from the $\text{Co}_3\text{O}_4/\text{La}_2\text{O}_2\text{CO}_3$ surface to CH_4 [26]. This is very beneficial for the CH_4 reaction process. In other respects, the presence of oxygen vacancies and the unique $\text{La}^{3+}\text{-O}^2$ -alkaline adsorption site of $\text{La}_2\text{O}_2\text{CO}_3$ form more reactive oxygen on the catalyst surface, making it easier for the adsorbed state CH_4 to react with it in the next step.

The charge density difference on the $\text{Co}_3\text{O}_4/\text{La}_2\text{O}_2\text{CO}_3$ surface was calculated to further understand the electron transfer mechanism of the structure (Fig. 5c). Significant charge transfer could be observed at the structural interface, with the Co_3O_4 surface showing significant charge density accumulation and the $\text{La}_2\text{O}_2\text{CO}_3$ surface showing significant charge density deficiency. Furthermore, the Bader charge result showed a transferred electron number of 1.37 e. The $\text{La}_2\text{O}_2\text{CO}_3$ acted as an electron donor and promoted the redox ability and reactivity of Co_3O_4 , facilitating the transfer of reactive oxygen species generated on the $\text{La}_2\text{O}_2\text{CO}_3$ surface to the Co_3O_4 surface, which enhanced the CH_4 adsorption and C-H bond breakage [54,64]. Meanwhile, the charge enrichment on the Co_3O_4 surface also made the Co-O bond energy lower and the Co 2p orbital shift to lower energy, which was consistent with the above analysis. The density of states (DOS) for Co_3O_4 and $\text{Co}_3\text{O}_4/\text{La}_2\text{O}_2\text{CO}_3$ showed (Fig. 5e-f) that the valence band center

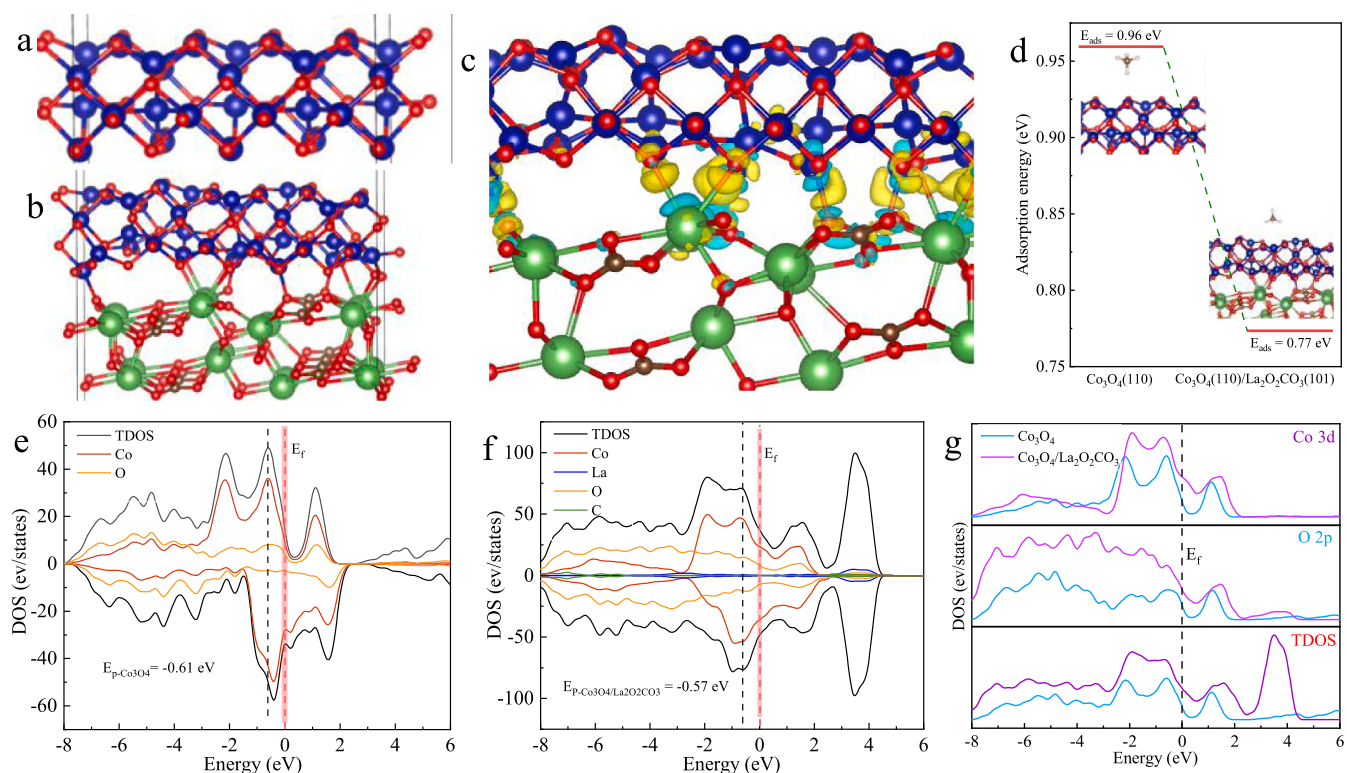


Fig. 5. Structural diagrams of (a) Co_3O_4 (110), (b) Co_3O_4 (110)/ $\text{La}_2\text{O}_2\text{CO}_3$ (110) with green, blue, red and brown spheres representing La, Co, O and C, respectively. (c) Difference in charge density on the Co_3O_4 (110)/ $\text{La}_2\text{O}_2\text{CO}_3$ (110) surface, the blue (yellow) area represents the absence of charge density. (d) Schematic adsorption energies (E_{ads}) for Co_3O_4 (110) and Co_3O_4 (110)/ $\text{La}_2\text{O}_2\text{CO}_3$ (110). (e) Co_3O_4 (110) and (f) Co_3O_4 (110)/ $\text{La}_2\text{O}_2\text{CO}_3$ (110) calculated DOSs. (g) Partial density of states (PDOS) for Co 3d and O 2p.

increased for $\text{Co}_3\text{O}_4/\text{La}_2\text{O}_2\text{CO}_3$ compared to Co_3O_4 , and the DOS peak ($E_{\text{p}} - \text{Co}_3\text{O}_4/\text{La}_2\text{O}_2\text{CO}_3 = 0.57$ eV) was closer to the Fermi level (E_f). This means that the introduction of $\text{La}_2\text{O}_2\text{CO}_3$ (101) gave Co_3O_4 a higher electron conduction efficiency, which resulted in enhanced electron transfer between the Co and O atoms. Moreover, Co and O partial density of states (PDOS) could be observed more around the Fermi level (Fig. 5g), which implied that Co-O bonds were more easily broken on the $\text{Co}_3\text{O}_4/\text{La}_2\text{O}_2\text{CO}_3$ surface and that the mobility of reactive oxygen species was also enhanced. In more detail, the structure also contributed to improving the electron transfer capability among the elements, the electrical conductivity of the material and the degree of surface ion diffusion [65,66]. These calculations provided additional theoretical basis for the characterization and tested catalytic performance described above. It also well explained the structure-function relationship of the $\text{Co}_3\text{O}_4/\text{La}_2\text{O}_2\text{CO}_3$ heterogeneous structured catalyst and the intrinsic mechanism of surface catalytic performance enhancement.

3.6. Exploring the mechanism of methane oxidation reaction

The *in situ* DRIFTS technique was used to confirm the adsorbed substances and reaction intermediates on the catalyst surface during the reaction to gain insight into the CH_4 reaction mechanism for this catalyst (Fig. 6). In the spectra of the LC-(0)C and LC-(0.9)C catalysts, the spectra changed increasing temperature. All samples demonstrated energy bands at 2900–3100 cm^{-1} corresponding to the C-H bond stretching vibration (ν) of gaseous CH_4 . Meanwhile, the C-H bond bending vibration (δ) was observed at 1300 cm^{-1} [22,67]. Asymmetric bending vibrations (δ_{as}) of CH_3 were also observed at 1370 cm^{-1} [21]. These peak intensities all gradually decreased with increasing reaction temperature, which provided direct evidence for CH_4 oxidation on the catalyst surface. The energy band near 2360 cm^{-1} represents the asymmetric stretching of the C=O bond in gas-phase CO_2 [68]. It was worth noting that the energy band change at 2360 cm^{-1} was very obvious with increasing reaction

temperature throughout the reaction, especially the change in the LC-(0.9)C catalyst from 350 °C to 400 °C, and the change in the LC-(0)C catalyst was weaker. This means that LC-(0.9)C had stronger oxygen mobility and more reactive oxygen than LC-(0)C. By 400 °C, the amount of CO_2 adsorbed on the surface of the LC-(0.9)C catalyst increased significantly, whereas the amount of CO_2 adsorbed on the surface of the LC-(0)C catalyst was very small. Simultaneously, bidentate and monodentate carbonate species were discovered at 856 and 1080 cm^{-1} , generated by CO_2 adsorption from CH_4 oxidation on the $\text{La}^{3+}\text{-O}^2-$ alkaline adsorption sites on the $\text{La}_2\text{O}_2\text{CO}_3$ surface, and the peaks decayed with increasing temperature [35,45]. This also provided direct evidence for the reaction of $\text{La}^{3+}\text{-O}^2-$ alkaline adsorption sites on the $\text{La}_2\text{O}_2\text{CO}_3$ surface with adsorbed CO_2 to generate bidentate and monodentate carbonates. The carbonate formed at the alkaline site interacted with gaseous oxygen to form more reactive oxygen species, and the interaction of the $\text{La}_2\text{O}_2\text{CO}_3$ surface carbonate with gaseous oxygen was accelerated as the temperature increased, resulting in reduced surface carbonate buildup. This was in good agreement with the O_2 and CO_3^{2-} conversion equilibrium and peroxy radical (O_2^\cdot) conversion proposed by Dubois et al. [69]:



The peaks near 1510 and 1460 cm^{-1} corresponded to formate and carbonate species produced by the catalytic reaction [21,47], which suggested that formate and carbonate were important intermediates in CH_4 oxidation. CH_4 would be destroyed by reactive oxygen species on the catalyst surface to form intermediate products, which would be further oxidized to CO_2 and H_2O . In addition, the overall signal intensity of LC-(0.9)C was higher than that of LC-(0)C, demonstrating that LC-(0.9)C had a stronger adsorption capacity for CH_4 and a faster decomposition rate of intermediates compared with LC-(0)C. *In situ*

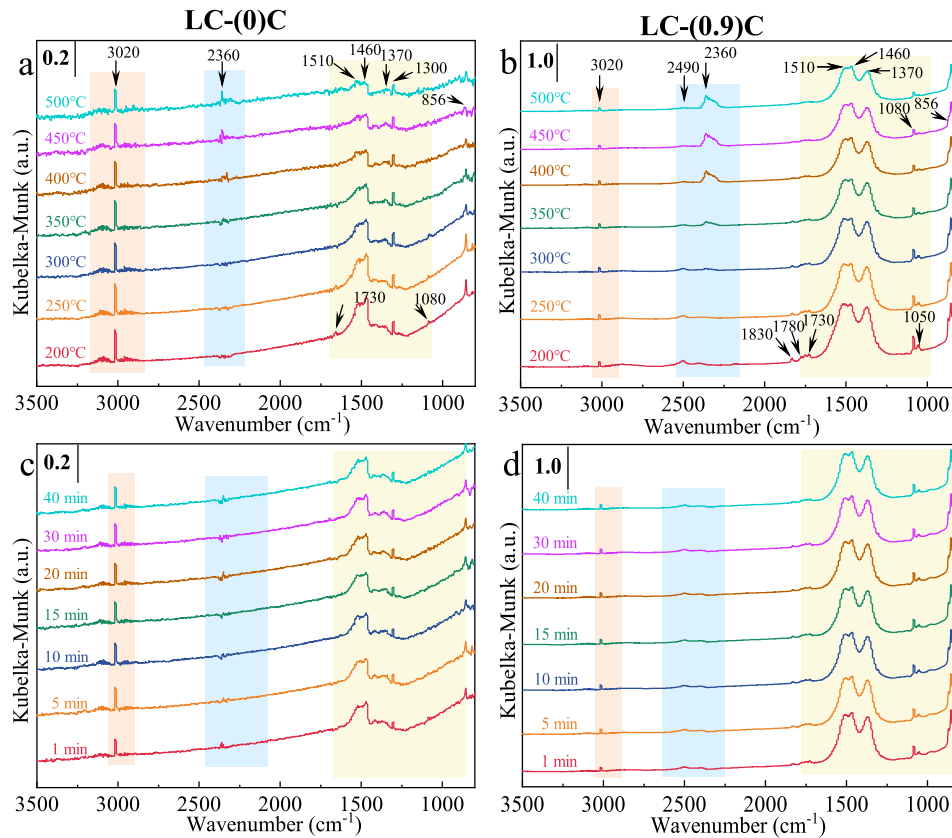


Fig. 6. *In situ* DRIFTS spectra of (a) LC-(0)C and (b) LC-(0.9)C at 200–500 °C, *In situ* DRIFTS spectra of (c) LC-(0)C and (d) LC-(0.9)C at 300 °C.

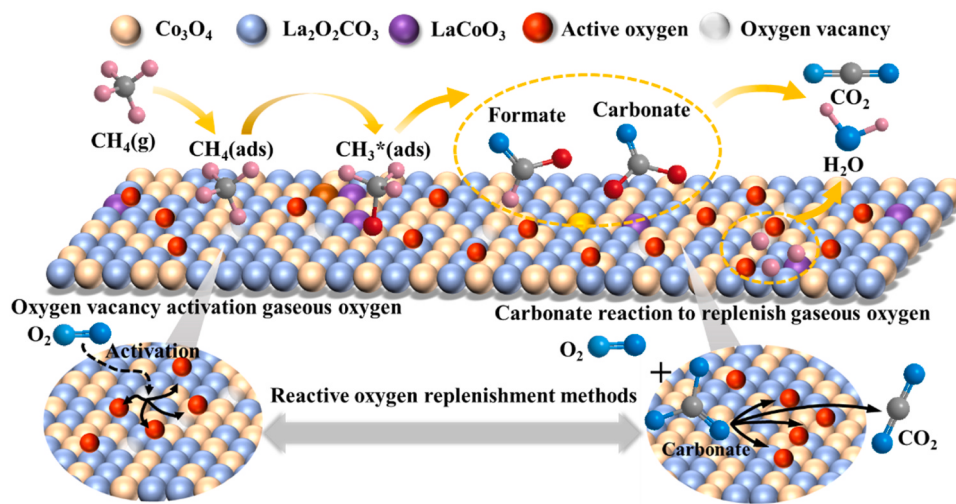


Fig. 7. CH₄ oxidation reaction process over LC-(0.9)C catalyst and source of reactive oxygen species.

spectra of LC-(0)C and LC-(0.9)C at 300 °C with time are shown in Fig. 6 c-d. None of the signal peaks were enhanced with increasing exposure time, especially the peaks corresponding to CH₄. This demonstrates that CH₄ does not accumulate excessively on the catalyst surface to obstruct the catalytic active site, which is conducive to a stable catalytic reaction. The CH₄ adsorption intensity at LC-(0.9)C was much higher than that at LC-(0)C, again indicating a greater affinity of LC-(0.9)C for the adsorption and activation of CH₄.

Based on the above characterization and *in situ* DRIFTS, it could be inferred that CH₄ follows the reaction path in this catalyst. (1) Gaseous CH₄ was first activated on the active site from the catalyst surface and then underwent surface adsorption, forming adsorbed state CH₄. CH₄ (ads) combined with reactive oxygen species, which destabilized the stable structure of CH₄ and formed reactive methyl radicals. (2) Methyl radicals were further destroyed by reactive oxygen species to form formate species and carbonate species. (3) Surface-active oxygen species were generated by adsorption of CO₂ generated from CH₄ oxidation on the La₂O₂CO₃ surface to generate carbonate species, which were then further reacted with gaseous oxygen to generate surface-active oxygen species. The activation of gaseous oxygen on the surface oxygen vacancy to form surface active oxygen is supplemented in two ways. (4) Carbonate and formate species then react rapidly with reactive oxygen species and deep oxidation occurs to produce CO₂ and H₂O.

4. Conclusions

In summary, Co₃O₄/La₂O₂CO₃/LaCoO₃ heterostructure catalysts (LC-(0.9)C) were synthesized using a simple solvent-thermal method applied to LaCoO₃ perovskite, and a suitable alcohol solvent (glycerol) and ratio were screened. The structure exhibited excellent low temperature catalytic activity, stability and resistance to poisoning and water. The reaction rate of LC-(0.9)C was almost 13 times higher than that of LC-(0)C and LC. A series of characterization results demonstrated that the excellent catalytic performance of the structure was attributed to the abundant production of defective oxygen species and high-valent active Co species. Notably, La₂O₂CO₃ provided more active oxygen to the Co₃O₄ surface through charge transfer, effectively improved the Co active site utilization. Meanwhile, it could be preferentially adsorbed on the La₂O₂CO₃ surface in the presence of water vapor and SO₂ to protect Co₃O₄ from poisoning. The Co₃O₄/La₂O₂CO₃ interface accelerated the charge transfer to the Co₃O₄ surface, caused the structure to exhibit more density states near the Fermi level, and enhanced the adsorption and dissociation of oxygen and CH₄, which further confirmed the above results. Combined characterization analysis and *in situ* DRIFTS results were used to infer the reaction pathway and reactive oxygen species

supplementation of LC-(0.9)C in the CH₄-catalyzed oxidation process. This oxide-rare earth carbonate heterostructure was proposed to provide a reliable strategy for the design and synthesis of low-cost, high-activity and resistant rare earth mixed oxide catalysts.

CRediT authorship contribution statement

Yahan Wang: Investigation, Methodology, Formal analysis, Writing – original draft, Writing – review & revision. **Saifei Wang:** Formal analysis, Funding acquisition, Writing – review & revision. **Jingyu Bai:** Methodology, Formal analysis. **Long Zhang:** Investigation, Writing – review & revision. **Shiguang Zhao:** Formal analysis, Writing – review & revision. **Jiguang Deng:** Resources, Supervision, Writing – review & revision. **Xiaolong Tang:** Resources, Supervision, Writing – review & revision. **Erhong Duan:** Resources, Supervision, Writing – review & revision, Funding acquisition.

Declaration of Competing Interest

The authors declare that they have no known competing financial interests or personal relationships that could have appeared to influence the work reported in this paper.

Data availability

Data will be made available on request.

Acknowledgments

This work was supported by National Natural Science Foundation of China (U20A20130), Natural Science Foundation of Hebei Province (B2022208040, B2021208033).

Appendix A. Supporting information

Supplementary data associated with this article can be found in the online version at doi:10.1016/j.apcatb.2023.123079.

References

- [1] Y.Q. Ding, Q.Q. Wu, B. Lin, Y.L. Guo, Y. Guo, Y.S. Wang, L. Wang, W.C. Zhan, Superior catalytic activity of a Pd catalyst in methane combustion by fine-tuning the phase of ceria-zirconia support, *Appl. Catal. B: Environ.* 266 (2020), 118631.
- [2] G. Caravaggio, L. Nossova, M.J. Turnbull, Nickel-magnesium mixed oxide catalyst for low temperature methane oxidation, *Chem. Eng. J.* 405 (2021), 126862.

- [3] R.J. Farrauto, Low-temperature oxidation of methane, *Science* 337 (2012) 659–660.
- [4] M.Y. Gao, Z.M. Gong, X.F. Weng, W.X. Shang, Y.C. Chai, W.L. Dai, G.J. Wu, N.J. Guan, L.D. Li, Methane combustion over palladium catalyst within the confined space of MFI zeolite, *Chin. J. Catal.* 42 (2021) 1689–1699.
- [5] L. Feng, P.I. Palmer, S.H. Zhu, R.J. Parker, Y. Liu, Tropical methane emissions explain large fraction of recent changes in global atmospheric methane growth rate, *Nat. Commun.* 13 (2022) 1378–1386.
- [6] J.H. Chen, H. Arandian, X. Gao, J.H. Li, Recent advances in catalysts for methane combustion, *Catal. Surv. Asia* 19 (2015) 140–171.
- [7] L. He, Y.L. Fan, J. Bellettre, J. Yue, L.G. Luo, A review on catalytic methane combustion at low temperatures: catalysts, mechanisms, reaction conditions and reactor designs, *Renew. Sust. Energ. Rev.* 119 (2020), 109589.
- [8] W.Z. Si, Y. Wang, S. Zhao, F.Y. Hu, J.H. Li, A facile method for in situ preparation of the Mn₂O₃/LaMnO₃ catalyst for the removal of toluene, *Environ. Sci. Technol.* 50 (2016) 4572–4578.
- [9] Y. Ma, L. Wang, J.Z. Ma, H.H. Wang, C.B. Zhang, H. Deng, H. He, Investigation into the enhanced catalytic oxidation of o-Xylene over MOF-derived Co₃O₄ with different shapes: The role of surface twofold-coordinate lattice oxygen (O_{2d}), *ACS Catal.* 11 (2021) 6614–6625.
- [10] G. Chai, W. Zhang, L.F. Liotta, M. Li, Y. Guo, A. Giroir-Fendler, Total oxidation of propane over Co₃O₄-based catalysts: elucidating the influence of Zr dopant, *Appl. Catal. B: Environ.* 298 (2021) 120606–120620.
- [11] Y.F. Jian, M.J. Tian, C. He, J.C. Xiong, Z.Y. Jiang, H. Jin, L.R. Zheng, R. Albilali, J.W. Shi, Efficient propane low-temperature destruction by Co₃O₄ crystal facets engineering: Unveiling the decisive role of lattice and oxygen defects and surface acid-base pairs, *Appl. Catal. B: Environ.* 283 (2021), 119657.
- [12] A. Choya, B. Rivas, J.I. Gutiérrez-Ortiz, R. López-Fonseca, On the effect of the synthesis route of the support in Co₃O₄/CeO₂ catalysts for the complete oxidation of methane, *Ind. Eng. Chem. Res.* 61 (2022) 17854–17865.
- [13] D.Y. Li, R.D. Xu, M.S. Tian, Y.W. Jia, Z.H. Gu, X. Zhu, Encapsulated Co₃O₄/(SiAl_xAl₂O₃) thermal storage functional catalysts for catalytic combustion of lean methane, *Appl. Therm. Eng.* 181 (2020), 116012.
- [14] H. Jeong, J. Bae, J.W. Han, H. Lee, Promoting effects of hydrothermal treatment on the activity and durability of Pd/CeO₂ catalysts for CO oxidation, *ACS Catal.* 7 (2017) 7097–7105.
- [15] H. Arandian, H.X. Dai, J.G. Deng, Y. Wang, H.Y. Sun, S.H. Xie, B.Y. Bai, Y.X. Liu, K. Ji, J.H. Li, Three-Dimensionally ordered macroporous La_{0.65}Sr_{0.4}MnO₃ supported Ag nanoparticles for the combustion of methane, *J. Phys. Chem. C* 114 (2014) 14913–14928.
- [16] L.T. Sun, X.L. Liang, H.M. Liu, H.J. Cao, X.H. Liu, Y. Jin, X.Y. Li, S. Chen, X.D. Wu, Activation of Co-O bond in {110} facet exposed Co₃O₄ by Cu doping for the boost of propane catalytic oxidation, *J. Hazard. Mater.* 452 (2023), 131319.
- [17] W.L. Zhang, M.Y. Li, X.T. Wang, X.W. Zhang, X.Y. Niu, Y.J. Zhu, Boosting catalytic toluene combustion over Mn doped Co₃O₄ spinel catalysts: Improved mobility of surface oxygen due to formation of Mn-O-Co bonds, *Appl. Surf. Sci.* 590 (2022), 153140.
- [18] A. Gremminger, P. Lott, M. Merts, M. Casapu, J.D. Grunwaldt, O. Deutschmann, Sulfur poisoning and regeneration of bimetallic Pd-Pt methane oxidation catalysts, *Appl. Catal. B: Environ.* 218 (2017) 833–843.
- [19] P. Lotta, M. Eck, D.E. Doronkin, A. Zimina, S. Tischer, R. Popescu, S. Belin, V. Bríois, M. Casapu, J.D. Grunwaldt, O. Deutschmann, Understanding sulfur poisoning of bimetallic Pd-Pt methane oxidation catalysts and their regeneration, *Appl. Catal. B: Environ.* 278 (2020), 119244.
- [20] S.H. Xie, Y.X. Liu, J.G. Deng, J. Yang, X.T. Zhao, Z. Han, K.F. Zhang, Y. Lu, F.D. Liu, H.X. Dai, Carbon monoxide oxidation over rGo-mediated gold/cobalt oxide catalysts with strong metal-support interaction, *ACS Appl. Mater. Interfaces* 12 (2020) 31467–31476.
- [21] Q. Li, N.J. Luo, D. Xia, P. Huang, X.B. Liu, T. Odoom-Wubah, J.L. Huang, G.L. Chai, D.H. Sun, Q.B. Li, Interfacial effects in CuO/Co₃O₄ heterostructures enhance benzene catalytic oxidation performance, *Environ. Sci. - Nano.* 9 (2022) 781–796.
- [22] S.M. Liu, W.J. Xue, Y.J. Ji, W.Q. Xu, W.X. Chen, L.H. Jia, T.Y. Zhu, Z.Y. Zhong, G.W. Xu, D.H. Mei, F.B. Su, Interfacial oxygen vacancies at Co₃O₄-CeO₂ heterointerfaces boost the catalytic reduction of NO by CO in the presence of O₂, *Appl. Catal. B: Environ.* 323 (2023), 122151.
- [23] L.X. Xu, Y. Pan, H.M. Li, R.C. Xu, Z.H. Sun, Highly active and water-resistant Lanthanum-doped platinum-cobalt oxide catalysts for CO oxidation, *Appl. Catal. B: Environ.* 331 (2023), 122678.
- [24] S.N. Lu, H.H. Song, Y.H. Xiao, K. Qadir, Y.Q. Li, Y.S. Li, G.H. He, Promoted catalytic activity of CO oxidation at low temperatures by tuning ZnO morphology for optimized CuO/ZnO catalysts, *Colloids Interface, Sci. Commun.* 57 (2023), 100698.
- [25] M. Honkanen, J.G. Wang, M. Kärkkäinen, M. Huuhtanen, H. Jiang, K. Kallinen, R. L. Keiski, J. Akola, V. Minnamari, Regeneration of sulfur-poisoned Pd-based catalyst for natural gas oxidation, *J. Catal.* 358 (2018) 253–256.
- [26] S. Yoon, J. Jo, B. Jeon, J. Lee, M.G. Cho, M.H. Oh, B. Jeong, T.J. Shin, H.Y. Jeong, J.Y. Park, T. Hyeon, Revealing charge transfer at the interface of spinel oxide and ceria during CO oxidation, *ACS Catal.* 11 (2021) 1516–1527.
- [27] J.A. Li, M.M. Li, P. Gui, L.N. Zheng, J.S. Liang, G. Xue, Hydrothermal synthesis of sandwich interspersed LaCO₃OH/Co₃O₄/graphene oxide composite and the enhanced catalytic performance for methane combustion, *Catal. Today* 327 (2019) 134–142.
- [28] M.S. Santos, R. Frety, L. Lisi, S. Cimino, S.T. Brandão, LaNi_{1-x}Co_xO₃ perovskites for methane combustion by chemical looping, *Fuel* 292 (2021), 120187.
- [29] H. Wang, H. Zhou, S.Q. Li, X. Ge, L. Wang, Z. Jin, C.T. Wang, J.B. Ma, X.F. Chu, X. J. Meng, W. Zhang, F.S. Xiao, Strong oxide-support interactions accelerate selective dehydrogenation of propane by modulating the surface oxygen, *ACS Catal.* 10 (2020) 10559–10569.
- [30] S.F. Wang, P.Q. Chu, J. Liu, C. Wang, E.H. Duan, J.G. Deng, L.A. Hou, Amino acid-deep eutectic solvents/LaCo₃ mutualism system: Forming La-Co-C-O hybrid for low temperature methane catalytic oxidation, *Fuel* 316 (2022), 123358.
- [31] M. Spiliopoulou, D.P. Triandafyllidis, A. Valmas, C. Kosinas, A.N. Fitch, R.B. V. Dreese, I. Margiolaki, Rietveld refinement for macromolecular powder diffraction, *Cryst. Growth Des.* 20 (2020) 8101–8123.
- [32] J.A. Wang, L.F. Chen, M.A. Valenzuela, A. Montoya, J. Salmones, P.D. Angel, Rietveld refinement and activity of CO oxidation over Pd/Ce_{0.8}Zr_{0.2}O₂ catalyst prepared via a surfactant-assisted route, *Appl. Surf. Sci.* 230 (2004) 34–43.
- [33] Y.H. Hou, W.C. Han, W.S. Xia, H.L. Wan, Structure sensitivity of La₂O₂CO₃ catalysts in the oxidative coupling of methane, *ACS Catal.* 5 (2015) 1663–1674.
- [34] Y.X. Li, W. Li, Y.Q. Lan, C. Chen, Bifunctional Co₃O₄-La₂O₂CO₃@C derived from MOFs for peroxyomonosulfate activation to degrade roxarsone and simultaneous removal of released inorganic arsenic from water, *Chem. Eng. J.* 432 (2022), 134426.
- [35] R. Feng, P.Y. Niu, Q. Wang, B. Hou, L.T. Jia, M.G. Lin, D.B. Li, In-depth understanding of the crystal-facet effect of La₂O₂CO₃ for low-temperature oxidative coupling of methane, *Fuel* 308 (2022), 121848.
- [36] Y.F. Jian, Z.Y. Jiang, C. He, M.J. Tian, W.Y. Song, G.Q. Gao, S.N. Chai, Crystal facet engineering induced robust and sinter-resistant Au/α-MnO₂ catalyst for efficient oxidation of propane: Indispensable role of oxygen vacancies and Au⁸⁺ species, *Catal. Sci. Technol.* 11 (2021) 1089–1097.
- [37] C. Zhang, J.G. Wang, S.F. Yang, H. Liang, Y. Men, Boosting total oxidation of acetone over spinel MCo₂O₄ (M = Co, Ni, Cu) hollow mesoporous spheres by cation-substituting effect, *J. Colloid Interf. Sci.* 539 (2019) 65–75.
- [38] G.G. Li, N. Li, Y.G. Sun, Y.M. Qu, Z.Y. Jiang, Z.Y. Zhao, Z.S. Zhang, J. Cheng, Z.P. Hao, Efficient defect engineering in Co-Mn binary oxides for low-temperature propane oxidation, *Appl. Catal. B: Environ.* 282 (2021) 119512–119522.
- [39] S.P. Rong, P.Y. Zhang, F. Liu, Y.J. Yang, Engineering crystal facet of α-MnO₂ nanowire for highly efficient catalytic oxidation of carcinogenic airborne formaldehyde, *ACS Catal.* 8 (2018) 3435–3446.
- [40] W.D. Zhang, C. Descorme, J.L. Valverde, A. Giroir-Fendler, Yttrium-modified Co₃O₄ as efficient catalysts for toluene and propane combustion: Effect of yttrium content, *J. Hazard. Mater.* 437 (2022), 129316.
- [41] G.T. Chai, W.D. Zhang, L.F. Liotta, M.Q. Li, Y.L. Guo, A. Giroir-Fendler, Total oxidation of propane over Co₃O₄-based catalysts: Elucidating the influence of Zr dopant, *Appl. Catal. B: Environ.* 298 (2021), 120606.
- [42] B. Cui, L.J. Zhou, K. Li, Y.Q. Liu, D. Wang, Y.Y. Ye, S.R. Li, Holey Co-Ce oxide nanosheets as a highly efficient catalyst for diesel soot combustion, *Appl. Catal. B: Environ.* 267 (2020), 118670.
- [43] W.J. Zhu, X. Chen, J.H. Jin, X. Di, C.H. Liang, Z.M. Liu, Insight into catalytic properties of Co₃O₄-CeO₂ binary oxides for propane total oxidation, *Chin. J. Catal.* 41 (2020) 679–690.
- [44] P. Huang, Y.H. Zhao, J. Zhang, Y. Zhu, Y.H. Sun, Exploiting shape effects of La₂O₃ nanocatalysts for oxidative coupling of methane reaction, *Nanoscale* 5 (2022) 10844–10848.
- [45] K. Li, X. Chang, C.L. Pei, X.Y. Li, S. Chen, X.H. Zhang, S. Assabumrungrat, Z. J. Zhao, L. Zeng, J.L. Gong, Ordered mesoporous Ni/La₂O₃ catalysts with interfacial synergism towards CO₂ activation in dry reforming of methane, *Appl. Catal. B: Environ.* 259 (2019), 118092.
- [46] Z.Q. Hou, L.Y. Dai, J.G. Deng, G.F. Zhao, L. Jing, Y.S. Wang, X.H. Yu, R.Y. Gao, X. R. Tian, H.X. Dai, D.S. Wang, Y.X. Liu, Electronically engineering water resistance in methane combustion with an atomically dispersed tungsten on PdO catalyst, *Angew. Chem. Int. Ed.* 134 (2022), e202201655.
- [47] S.P. Wu, H.M. Liu, Z. Huang, H.L. Xu, W. Shen, O-vacancy-rich porous MnO₂ nanosheets as highly efficient catalysts for propane catalytic oxidation, *Appl. Catal. B: Environ.* 312 (2022), 121387.
- [48] H. Zhang, T.Y. Gao, Q. Cao, W.H. Fang, Tailoring the reactive oxygen species in mesoporous NiO for selectivity-controlled aerobic oxidation of 5-hydroxymethyl-furfural on a loaded Pt catalyst, *ACS Sustain. Chem. Eng.* 9 (2021) 6056–6067.
- [49] J.W. Xu, Y. Zhang, X.L. Xu, X.Z. Fang, R. Xi, Y.M. Liu, R.Y. Zheng, X. Wang, Constructing La₂B₂O₇ (B = Ti, Zr, Ce) compounds with three typical crystalline phases for the oxidative coupling of methane: The effect of phase structures, superoxide anions, and alkalinity on the reactivity, *ACS Catal.* 9 (2019) 4030–4045.
- [50] S.B. Wang, L.N. Cong, C.C. Zhao, Y.T. Li, Y.Q. Pang, Y.H. Zhao, S.G. Li, Y.H. Sun, First principles studies of CO₂ and O₂ chemisorption on La₂O₃ surfaces, *Phys. Chem. Chem. Phys.* 19 (2017) 26799–26811.
- [51] X.Y. Huang, C.X. Dang, H. Yu, H.J. Wang, F. Peng, Morphology effect of Ir/ La₂O₂CO₃ nanorods with selectively exposed {110} facets in catalytic steam reforming of glycerol, *ACS Catal.* 5 (2015) 1155–1163.
- [52] A. Olafsen, A.K. Larsson, H. Fjellvåg, B.C. Hauback, On the crystal structure of Ln₂O₂CO₃ II (Ln = La and Nd), *J. Solid. State Chem.* 158 (2001) 12–24.
- [53] C.Q. Chu, Y.H. Zhao, S.G. Li, Y.H. Sun, CO₂ chemisorption and its effect on methane activation in La₂O₃-catalyzed, Oxid. coupling methane, *J. Phys. Chem. C* 120 (2016) 2737–2746.
- [54] Q. Zhao, Q.L. Liu, Y.F. Zheng, R. Han, C.F. Song, N. Ji, D.G. Ma, Enhanced catalytic performance for volatile organic compound oxidation over in-situ growth of MnO_x on Co₃O₄ nanowire, *Chemosphere* 244 (2020), 125532.
- [55] F.Y. Hu, Y. Peng, J.J. Chen, S. Liu, H. Song, J.H. Li, Low content of CoO_x supported on nanocrystalline CeO₂ for toluene combustion: the importance of interfaces between active sites and supports, *Appl. Catal. B: Environ.* 240 (2019) 329–336.
- [56] C. Feng, Q.Q. Gao, G.Y. Xiong, Y.F. Chen, Y. Pan, Z.Y. Fei, Y.P. Li, Y.K. Lu, C.G. Liu, Y.Q. Liu, Defect engineering technique for the fabrication of LaCo₃O₇ perovskite

- catalyst via urea treatment for total oxidation of propane, *Appl. Catal. B: Environ.* 304 (2022), 121005.
- [57] X.Y. Wang, X.B. Peng, H.Y. Ran, B.Y. Lin, J. Ni, J.X. Lin, L.L. Jiang, Influence of Ru substitution on the properties of LaCo₃O₄ catalysts for ammonia synthesis: XAFS and XPS studies, *Ind. Eng. Chem. Res.* 57 (2018) 17375–17383.
- [58] K. Zeng, X.Y. Li, C. Wang, Z. Wang, P. Guo, J. Yu, C.H. Zhang, X.S. Zhao, Three-dimensionally macroporous MnZrO_x catalysts for propane combustion: Synergistic structure and doping effects on physicochemical and catalytic properties, *J. Colloid Interface Sci.* 572 (2020) 281–296.
- [59] C.P. Shan, Y. Zhang, Q. Zhao, K.X. Fu, Y.F. Zheng, R. Han, C.X. Liu, N. Ji, W. C. Wang, Q.L. Liu, Acid etching-induced *in situ* growth of λ -MnO₂ over CoMn spinel for low-temperature volatile organic compound oxidation, *Environ. Sci. Technol.* 56 (2022) 10381–10390.
- [60] X. Yuan, L.Q. Meng, Z.W. Xu, C.H. Zheng, H.B. Zhao, CuO quantum dots supported by SrTiO₃ perovskite using the flame spray pyrolysis method: Enhanced activity and excellent thermal resistance for catalytic combustion of CO and CH₄, *Environ. Sci. Technol.* 55 (2021) 14080–14086.
- [61] G. Chen, D.S. Hong, H.Q. Xia, W. Sun, S.J. Shao, B.W. Gong, S. Wang, J.Y. Wu, X. Y. Wang, Q.G. Dai, Amorphous and homogeneously Zr-doped MnO_x with enhanced acid and redox properties for catalytic oxidation of 1,2-Dichloroethane, *Chem. Eng. J.* 428 (2022), 131067.
- [62] J.M. Bea, D.J. Shin, H.J. Jeong, B.S. Kim, J.W. Han, H.J. Lee, Highly water-resistant La-doped Co₃O₄ catalyst for CO oxidation, *ACS Catal.* 9 (2019) 10093–10100.
- [63] W.G. Han, F. Dong, W.L. Han, J.F. Yao, Y. Meng, Z.C. Tang, A new strategy for designing highly efficient Co₃O₄ catalyst with the molecular space configurations for toluene catalytic combustion, *Chem. Eng. J.* 2 (2022), 134953.
- [64] K.A. Sun, Y.Q. Liu, Y. Pan, H.Y. Zhu, J.C. Zhao, L.Y. Zeng, Z. Liu, C.G. Liu, Targeted bottom-up synthesis of 1T-phase MoS₂ arrays with high electrocatalytic hydrogen evolution activity by simultaneous structure and morphology engineering, *Nano Res.* 11 (2018) 4368–4379.
- [65] C.P. Wang, Y. Feng, H. Sun, Y.R. Wang, J. Yin, Z.P. Yao, X.H. Bu, J. Zhu, Self-optimized metal-organic framework electrocatalysts with structural stability and high current tolerance for water oxidation, *ACS Catal.* 11 (2021) 7132–7143.
- [66] W.J. Yang, Y.F. Zhu, F. You, L. Yan, Y.J. Ma, C.Y. Lu, P.Q. Gao, Q. Hao, W.L. Li, Insights into the surface-defect dependence of molecular oxygen activation over birnessite-type MnO₂, *Appl. Catal. B: Environ.* 233 (2018) 184–193.
- [67] L.C. Chen, J.B. Jia, R. Ran, X.P. Song, Nickel doping MnO₂ with abundant surface pits as highly efficient catalysts for propane deep oxidation, *Chem. Eng. J.* 369 (2019) 1129–1137.
- [68] D.W. Han, X.Y. Ma, X.Q. Yang, M.L. Xiao, H. Sun, L.J. Ma, X.L. Yu, M.F. Ge, Metal organic framework-templated fabrication of exposed surface defect-enriched Co₃O₄ catalysts for efficient toluene oxidation, *J. Colloid Interf. Sci.* 603 (2021) 695–705.
- [69] J.L. Dubois, M. Bisiaux, H. Mimoun, C.J. Cameron, X-Ray photoelectron spectroscopic studies of lanthanum oxide based oxidative coupling of methane catalysts, *Chem. Lett.* 6 (1990) 967–970.